This article has been accepted for publication in a future issue of this journal, but has not been fully edited. Content may change prior to final publication. Citation information: DOI 10.1109/TUFFC.2018.2856301, IEEE Transactions on Ultrasonics, Ferroelectrics, and Frequency Control

Fourier Domain Beamforming and Structure-Based Reconstruction for Plane-Wave Imaging

Tanya Chernyakova*[a] *Student Member, IEEE*, Regev Cohen*[a] *Student Member, IEEE*, Rotem Mulayoff*, Yael Sde-Chen*, Christophe Fraschini**, Jeremy Bercoff ** and Yonina C. Eldar* *Fellow, IEEE*
*Department of Electrical Engineering, Technion, Israel Institute of Technology, Haifa, Israel
**Supersonic Imagine, Aix-en-Provence, France

***Abstract*—Ultrafast imaging based on coherent plane-wave compounding is one of the most important recent developments in medical ultrasound. It significantly improves image quality and allows for much faster image acquisition. This technique, however, requires large computational loads motivating methods for sampling and processing rate reduction. In this work we extend the recently proposed frequency domain beamforming (FDBF) framework to plane-wave imaging. Beamforming in frequency yields the same image quality while using fewer samples. It achieves at least 4 fold sampling and processing rate reduction by avoiding oversampling required by standard processing. To further reduce the rate we exploit the structure of the beamformed signal and use compressed sensing methods to recover the beamformed signal from its partial frequency data obtained at a sub-Nyquist rate. Our approach obtains 10 fold rate reduction compared to standard time domain processing. We verify performance in terms of spatial resolution and contrast based on scans of a tissue mimicking phantom obtained by a commercial Aixplorer system. In addition, *in vivo* carotid and thyroid scans processed using standard beamforming and FDBF are presented for qualitative evaluation and visual comparison. Finally, we demonstrate the use of FDBF for shear-wave elastography by generating velocity maps from beamformed data processed at sub-Nyquist rates.**

***Index Terms*—Plane wave, array processing, beamforming compressed sensing, ultrasound.**

I. Introduction

Ultrasound is a radiation free imaging modality with numerous applications. The image is usually comprised of multiple scanlines, obtained by sequential insonification of the medium using focused acoustic beams. Thus, in most commercial systems today the number of transmissions is dictated by the number of scanlines comprising the image. As a result, the frame rate is limited to several tens of frames per second which is insufficient for a number of applications including echocardiography for heart motion analysis, 3D/4D imaging and elastography.

The key to frame rate improvement without compromising image quality is to break the link between the number of transmissions and the number of scanlines. An obvious way to reduce the number of transmissions is to insonify the entire scene with a pulsed plane-wave. The image lines are then obtained in parallel from the acquired data by standard dynamic beamforming upon reception. This approach was successfully applied by Fink and co-authors [1], [2] for real-time elastography, namely, imaging of the propagation of shear mechanical waves, implying ultrafast frame rates. However, due to inherent lack of focusing upon transmission, this method suffers from reduced contrast and resolution. One approach to overcome this limitation is by sequential transmission of several tilted plane-waves [3]. The images obtained from each insonification are added coherently to yield a final compounded image. The result is characterized by significantly improved resolution and contrast since coherent compounding effectively generates a posteriori synthetic focusing in the transmission [3].

Coherent plane wave compounding provides a framework for significant frame rate reduction while retaining image quality. This method, however, is challenging due to the high data transfer rates and large computational load. To achieve ultrafast imaging, all image lines are computed in parallel, typically on a software based platform. This implies that sampled raw radio frequency signals, detected at each array element, are directly transferred to the processing unit. Each image line is obtained by standard time domain beamforming, implying sampling rates that are much higher than the Nyquist rate of the detected signals. Rates up to 4-10 times the central frequency of the transmitted pulse are used in order to eliminate artifacts caused by digital implementation of beamforming in time [4]. Taking into account the number of transducer elements, up to 10^7 samples need to be transferred and digitally processed in real time to obtain an image. The processing unit, therefore, must be powerful enough to allow for real time beamforming.

One approach to reduce sampling rate is by quadrature sampling [5]. Here the signals are sampled at rates dictated by the RF (radio-frequency) Nyquist condition and then digitally demodulated and decimated to the effective Nyquist rate defined by the signals bandpass bandwidth. The resulting in-phase (I) and quadrature (Q) components are then used for further processing. Digital IQ demodulation and decimation require multiplication by complex exponentials and low-pass filtering of each sampled signal, thus increasing the overall computational load. Moreover, elastography, one of the main applications of ultrafast imaging, requires RF ultrasound data for tissue deformation calculations [6]–[8]. Therefore, alternatives for sampling and processing rate reduction are of high interest and can lead to simpler and cheaper systems. They

[a] These two authors contributed equally.

[b] This project has received funding from the European Union's Horizon 2020 research and innovation program under grant agreement No. 646804-ERC-COG-BNYQ.

This article has been accepted for publication in a future issue of this journal, but has not been fully edited. Content may change prior to final publication. Citation information: DOI 10.1109/TUFFC.2018.2856301, IEEE Transactions on Ultrasonics, Ferroelectrics, and Frequency Control

may also serve as a potential enabler for the concept of a wireless probe and remote processing [9].

A. Related Work

In focused mode a number of strategies exploiting signal structure and relying on compressed sensing (CS) techniques [10], [11] have been proposed for data rate reduction. These methods either allow for sampling and recovery of each individual detected signal at a low rate assuming sufficiently high SNR [12]–[15] or deal with recovering a beamformed signal from its low-rate samples [16]–[19]. The latter require access to the continuous-time beamformed data while in practice the beamformed signal is formed digitally at a high rate from samples of each of the individual received signals.

A practical method to acquire low-rate beamformed data from low-rate samples of the received signals in order to visualize macroscopic perturbations in the tissue was first suggested in [20] and was later extended to ultrafast imaging in [21]. A significant drawback of this approach is that the solution is approximated using orthogonal matching pursuit which fails to restore weak reflectors and leads to loss of speckle [22]. An improved technique, enabling sub-Nyquist data acquisition from each transducer element and low-rate processing, was presented in [22] to visualize all tissue components, namely both strong reflectors and weak scattered echoes. A generalization to 3D imaging was proposed in [23].

This sub-Nyquist approach is based on frequency domain beamforming (FDBF) where the computations can be carried out from less data samples. The Fourier components of the beamformed signal are computed as a weighted average of those of the individual detected signals. The weights are obtained through a distortion function that transfers the nonlinear time dependent beamforming delays to the frequency domain. Since the beam is obtained directly in frequency, its Fourier components are computed only within its effective bandwidth. When all the beam's Fourier coefficients within its bandwidth are computed, the sampling and processing rates are equal to the effective Nyquist rate [10]. In this case the oversampling required by time domain implementation of digital beamforming [4] is avoided leading to 4-10 fold rate reduction. The beam in time is then recovered by an inverse Fourier transform.

When further rate reduction is required, only a subset of the beam's Fourier coefficients is obtained, implying that the detected signals are sampled and processed at a sub-Nyquist rate. Recovery then relies on CS methods that exploit an appropriate model of the beam to compensate for the lack of frequency data. Low-rate data acquisition is based on the ideas of Xampling [12], [24], [25], which obtains the Fourier coefficients of individual detected signals from their low-rate samples.

B. Contributions

This work extends the FDBF framework to plane-wave imaging, expanding on the initial results we presented in [26]. In particular, we provide a detailed theoretical derivation of the proposed method and show experimental results including both phantom and *in vivo* acquisitions. We also consider the combination of FDBF and ℓ_1 based recovery for sub-Nyquist processing and its use for B-mode and elastography.

Besides the adjustment to the geometry of plane-wave transmissions, dynamic aperture and apodization are introduced to FDBF and implemented directly in frequency. The importance of dynamic aperture in plane-wave imaging stems from the fact that a relatively shallow depth is of interest. In the far field the lateral resolution is improved as the aperture increases, while under near field conditions the opposite occurs. Dynamic focusing approximately brings far field conditions to the near field, rendering the large aperture beneficial for all ranges. However, at ranges smaller than the size of the physical aperture of the transducer, which is typically the case for plane-wave imaging, it is challenging to maintain focus even with digital dynamic focusing. As a result, the optimal aperture size varies and should be increased dynamically with range [27]. Dynamic aperture ensures a constant F-number, denoted $f\#$, defined as the depth of focus in the tissue divided by the aperture width. This results in a more homogeneous beampattern throughout the entire image depth. In this case the apodization applied to improve contrast by reducing the side-lobes of the resulting beampattern is also dynamic. Explicitly, the window function used for weighting the transducer elements increases dynamically with range.

Since in Fourier domain processing we do not have access to time samples of the detected signals, we apply dynamic aperture and apodization on frequency samples. To this end we first express the aperture and apodization as time-dependent weight functions multiplying each detected signal. We then apply them directly in frequency through appropriate modification of the distortion function. As shown in [20], [22], an efficient implementation of FDBF is obtained through an appropriate approximation which relies on the decay property of the distortion function. We verify numerically that this is retained in plane wave imaging with dynamic aperture and apodization, and study the performance of FDBF for different approximation levels.

Translation of beamforming into the frequency domain allows sampling and processing signals at their effective Nyquist rate, which implies a 4 fold rate reduction. We next apply sub-Nyquist processing when only a portion of the beam's bandwidth is obtained by FDBF. This implies 10 fold rate reduction compared to the minimal rate required for time domain beamforming. To compensate for the lack of frequency data, we rely on the assumption that a typical ultrasound image is relatively sparse or compressible, namely, comprised of a small number of strong reflectors and much weaker sub-wavelength scatterers in the scanned tissue. The recovery in this case is formulated as an ℓ_1 optimization problem that is solved using CS methods. The performance is evaluated in terms of contrast and spatial resolution, where we use scans of a tissue mimicking phantom obtained by a commercial Aixplorer scanner. The application of the proposed method on *in vivo* carotid and thyroid scans allows for qualitative evaluation and visual comparison of images obtained using standard processing and FDBF with a 10 fold rate reduction. Finally, we perform shear-wave elastography (SWE) [2] using

This article has been accepted for publication in a future issue of this journal, but has not been fully edited. Content may change prior to final publication. Citation information: DOI 10.1109/TUFFC.2018.2856301, IEEE Transactions on Ultrasonics, Ferroelectrics, and Frequency Control

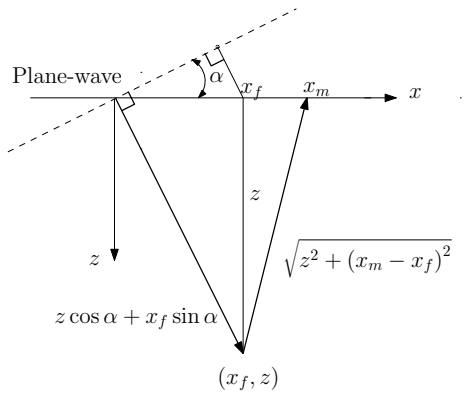

Fig. 1: Plane-wave imaging setup: a transducer is aligned along the x axis transmitting a propagating plane-wave with inclination α.

the data obtained by sub-Nyquist FDBF, demonstrating the potential for low-rate velocity estimation.

We note that CS reconstruction in time and frequency for plane-wave imaging was recently studied by several groups to reduce the number of transducers, the number of transmitted plane-waves and to improve image quality. In particular, a Fourier domain formulation of Green's function combined with CS recovery is presented in [28] and is shown to improve image quality for a single plane-wave transmission. In [29] time domain compressive beamforming is used to reconstruct point reflectors from a reduced number of receiving elements. In [30], Besson et al. consider limited diffraction beam theory [31], [32] applied to plane-wave acquisition in order to compute non-uniform frequency samples of an underlying image. Image reconstruction from its non-uniform spectrum is viewed as an ill-posed inverse problem, while solving it using CS leads to notable improvement of image quality. In contrast to the above works, we aim at reducing the amount of data required to obtain a clinically meaningful image. To this end we exploit the ability of CS to recover a signal from its low-rate measurements.

The rest of the paper is organized as follows: in Section II we review the processing performed in plane-wave imaging. In Section III we derive the proposed frequency domain formulation and verify its performance. Sub-Nyquist processing and sparsity based recovery are presented in Section IV.

II. Coherent Plane-Wave Compounding

In coherent plane-wave compounding, the final image is a result of coherently adding several images obtained by transmitting tilted plane-waves with different angles [3]. We begin with a description of beamforming applied upon reception to obtain each one of the images being compounded and then discuss the required computational load.

A. Time Domain Processing

Assume we transmit a plane-wave with inclination α as shown in Fig. 1. An echo reflected by a scatterer positioned at (x_f, z) arrives at a transducer element placed at x_m at time

$$\tau_m(z; x_f, \alpha) = \frac{1}{c}\left(z\cos\alpha + x_f\sin\alpha + \sqrt{z^2 + (x_m - x_f)^2}\right). \tag{1}$$

Beamforming involves averaging the signals detected by M transducer elements, $\{\varphi_m^\alpha(t)\}_{m=1}^M$, while compensating for the differences in arrival time. This results in a signal containing the energy reflected from the point (x_f, z). Using (1) and substituting $z = \frac{ct}{2}$, the beamformed signal, corresponding to an image line at lateral position x_f is given by

$$\Phi(t; x_f, \alpha) = \sum_{m=1}^{M} w_m(t; x_f)\hat{\varphi}_m(t; x_f, \alpha), \tag{2}$$

where

$$\hat{\varphi}_m(t; x_f, \alpha) = \varphi_m^\alpha(\tau_m(t; x_f, \alpha)), \tag{3}$$
$$\tau_m(t; x_f, \alpha) = \frac{1}{2}\left(t\cos\alpha + 2\frac{x_f}{c}\sin\alpha + \sqrt{t^2 + 4\delta_{fm}^2}\right).$$

Here $\delta_{fm} = |x_m - x_f|/c$ and $w_m(t; x_f)$ is a time-dependent weight-function multiplying each detected signal. Weight-functions are introduced to apply dynamic aperture and apodization as will be elaborated on further below. The final image with improved quality is obtained by coherent summation, so that the x_f-line in the final image is given by

$$\Phi(t; x_f) = \sum_{\alpha} \Phi(t; x_f, \alpha). \tag{4}$$

As mentioned in the introduction, the size of the active aperture, $M(z)$, namely the number of elements contributing to the beamforming summation in (2), should increase dynamically with the range z. This is done in a way that the ratio between the range and the size of the active aperture, denoted by the F-number, $f\#$, is constant, insuring a homogeneous beampattern throughout the entire image depth. The value of $f\#$ depends on the array directivity and usually varies between 1 and 2. Lower values of $f\#$ insure better focusing [33] but limit the range where $f\#$ can be kept constant. For a chosen value $f\#$ the size of the active aperture as a function of z is $M(z) = \frac{z}{f\#}$. Using $z = \frac{ct}{2}$, we can rewrite $M(z)$ as a function of time

$$M(t) = \frac{ct}{2f\#}. \tag{5}$$

Thus, for an image line x_f, the mth element is active only for

$$|x_m - x_f| \le \frac{M(t)}{2}, \tag{6}$$

i.e. at time $t \ge 4f\#\delta_{fm}$.

To improve contrast by reducing side-lobes, the active aperture is multiplied by an apodization window. The window function is dynamically scaled with range to fit the size of the active aperture. Thus, for an arbitrary apodization function each element in the active aperture is multiplied by a time dependent value $A_m(t; x_f)$. The overall weight function including both dynamic aperture and apodization is given by

$$w_m(t; x_f) = A_m(t; x_f)\mathrm{H}(t - 4f\#\delta_{fm}), \tag{7}$$

This article has been accepted for publication in a future issue of this journal, but has not been fully edited. Content may change prior to final publication. Citation information: DOI 10.1109/TUFFC.2018.2856301, IEEE Transactions on Ultrasonics, Ferroelectrics, and Frequency Control

where $\mathrm{H}(t)$ is a unit step function.

When expressed as a weight-function multiplying each detected signal, the dynamic aperture and apodization can be incorporated into FDBF and applied directly in frequency as we will see in Section III.

B. Computational Load

The beamforming process described in (2) is carried out digitally, rather than by manipulation of the analog signals. The signals detected at each element must be sampled at a sufficiently high rate to apply high-resolution time shifts. In practice, the signal is sampled at rates significantly higher than its Nyquist rate, in order to improve the system's beamforming resolution and to avoid artifacts caused by digital implementation of beamforming in time. Such a beamforming rate, f_s, usually varies from 4 to 10 times the transducer central frequency [4], [22]. Taking into account that the effective bandpass bandwidth in medical ultrasound is usually on the order of the central frequency, the detected signals are 4-10 times oversampled compared to the effective Nyquist rate. To avoid confusion, by effective Nyquist rate we mean the signal's effective bandpass bandwidth.

Since all the image lines are obtained in parallel, the process described in (2) is performed hundreds of times per plane-wave transmission. Therefore the computational load is significantly increased compared to standard focused imaging, where each transmission usually requires a single beamforming step. As a result, sampling and processing rate reduction are of high importance in plane-wave imaging.

To reduce the load and promote real-time implementation of ultrafast imaging we adopt the ideas of beamforming in frequency. As we show, in this domain the computations can be carried out from less data samples.

III. Frequency Domain Processing

To derive the expression for beamforming in frequency using low-rate samples in plane-wave mode, we need to account for the geometry of plane-wave transmission as well as introduce dynamic aperture and apodization. Explicitly, we show that despite the non-linear time-dependent nature of beamforming delays and time dependent weights defined in (2) and (3), the Fourier coefficients of the beam can be computed from the Fourier transform of the detected signals' low-rate samples.

A. Frequency-Domain Implementation

Following [22], we assume that the support of $\varphi_m^\alpha(t)$ is contained in $[0,T)$ where T is defined by the transmitted pulse penetration depth. Hence, the support of $\Phi(t;x_f,\alpha)$ is limited to $[0,T_B(x_f))$ where $T_B(x_f)$ is defined as

$$T_B(x_f) = \min_{1\le m\le M} \tau_m^{-1}(T;x_f,\alpha) \tag{8}$$

with $\tau_m^{-1}(t;x_f,\alpha)$ being the inverse of $\tau_m(t;x_f,\alpha)$.

Denote the Fourier series coefficients of $\Phi(t;x_f,\alpha)$ with respect to the interval $[0,T)$ by

$$\begin{aligned} c^\alpha[k] =& \frac{1}{T}\int_0^T \Phi(t;x_f,\alpha) I_{[0,T_B(x_f))}(t) e^{-i\frac{2\pi}{T}kt}dt \\ =& \sum_{m=1}^M \hat{c}_m^\alpha[k], \end{aligned} \tag{9}$$

where $I_{[a,b)}(t)$ is the indicator function, taking the value 1 for $a\le t\le b$ and 0 otherwise. From (3), we have

$$\begin{aligned} &\hat{c}_m^\alpha[k] = \\ &\frac{1}{T}\int_0^T \varphi_m^\alpha(\tau_m(t;x_f,\alpha)) w_m(t;x_f) I_{[0,T_B(x_f))}(t) e^{-i\frac{2\pi}{T}kt}dt. \end{aligned} \tag{10}$$

The idea of FDBF is to obtain frequency components of the beamformed signal without access to its time domain samples using the Fourier coefficients of non-delayed detected signals. The latter are provided by a low-rate Xampling scheme. We aim, therefore, to derive a relationship between the Fourier coefficients of the beam $\Phi(t;x_f,\alpha)$ and those of the detected signals. After algebraic manipulation on (10) similar to [20] we obtain

$$\hat{c}_m^\alpha[k] = \frac{1}{T}\int_0^T \varphi_m^\alpha(t) q_{k,m}(t;x_f,\alpha) e^{-i\frac{2\pi}{T}kt}dt. \tag{11}$$

The expression for $q_{k,m}(t;x_f,\alpha)$ is derived and presented in Appendix . Note that the delays and weighting of every signal $\varphi_m^\alpha(t)$ are effectively applied through the distortion function $q_{k,m}(t;x_f,\alpha)$.

We next replace $\varphi_m^\alpha(t)$ by its Fourier coefficients. Denoting the nth Fourier coefficient by $c_m^\alpha[n]$ we can rewrite (11) as

$$\begin{aligned} \hat{c}_m^\alpha[k] &= \sum_n c_m^\alpha[n] \frac{1}{T}\int_0^T q_{k,m}(t;x_f,\alpha) e^{-i\frac{2\pi}{T}(k-n)t}dt \\ &= \sum_n c_m^\alpha[k-n] Q_{k,m;x_f,\alpha}[n], \end{aligned} \tag{12}$$

where $Q_{k,m;x_f,\alpha}[n]$ are the Fourier coefficients of the distortion function with respect to $[0,T)$. When substituted by its Fourier coefficients, the distortion function effectively transfers the beamforming delays defined in (3) as well as dynamic aperture and apodization to the frequency domain. The function $q_{k,m}(t;x_f,\alpha)$ depends only on the array geometry and is independent of the received signals. Therefore, its Fourier coefficients can be computed off-line and used as a look-up-table (LUT) during the imaging cycle.

For apodization in our experiments we use a normalized Hamming window given by

$$A_m(t;x_f) = \frac{2f\#}{\left(a^2+\frac{1}{2}b^2\right)ct}\left(a + b\cos\left(4\pi f\#\delta_{fm}/t\right)\right), \tag{13}$$

with $a = 0.54, b = 0.46$. An explicit expression for the resulting distortion function $q_{k,m}(t;x_f,\alpha)$ for $\alpha \neq 0$ is given in Appendix . The analytical analysis of this expression is quite involved. Numerical studies show that most of the energy of the set $\{Q_{k,m;x_f,\alpha}[n]\}$ is concentrated around the dc component. This behavior is typical to any choice of k, m, x_f or α and is illustrated in Fig. 2. We therefore rewrite (12)

This article has been accepted for publication in a future issue of this journal, but has not been fully edited. Content may change prior to final publication. Citation information: DOI 10.1109/TUFFC.2018.2856301, IEEE Transactions on Ultrasonics, Ferroelectrics, and Frequency Control

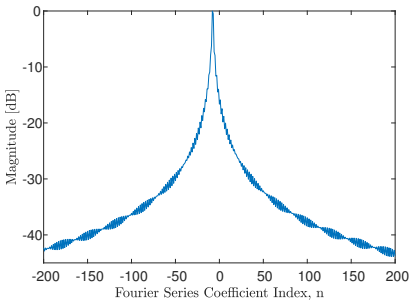

Fig. 2: Illustration of the rapid decay of the Fourier coefficients $\{Q_{k,m;x_f,\alpha}[n]\}$ of $q_{k,m}(t;x_f,\alpha)$ around the dc component for Hamming apodization.

with a finite number N_q of Q-coefficients as

$$\hat{c}_m^{\alpha}[k] \simeq \sum_{n=-N_1}^{N_2} c_m^{\alpha}[k-n]Q_{k,m;x_f,\alpha}[n], \tag{14}$$

where $N_q = N_2 + N_1 + 1$. The choice of N_1 and N_2 controls the approximation quality. The dependence of image quality on N_q is evaluated and presented in Section III-B for $N_q = 21, 11$ and 5.

Substitution of (14) into (9) yields the desired relationship between the Fourier coefficients of the beam and the individual signals

$$c^{\alpha}[k] \simeq \sum_m \sum_{n=-N_1}^{N_2} c_m^{\alpha}[k-n]Q_{k,m;x_f,\alpha}[n]. \tag{15}$$

The compounding is then performed directly in frequency

$$c[k] = \sum_{\alpha} c^{\alpha}[k], \tag{16}$$

where $c[k]$ denotes the Fourier coefficients of the x_f-line in the final image $\Phi(t;x_f)$ defined in (4). Applying an inverse Fourier transform on $\{c[k]\}$ yields the beamformed signal in time.

B. Performance Validation

We verify FDBF on data acquired by a Supersonic Imagine Aixplorer scanner. The images are produced with a 1D linear array, model SL 15-4, of 256 elements with central frequency $f_c = 9$ MHz and pitch 0.2 mm. Each image was obtained using 41 plane-wave transmissions with a separation of 1°. Standard time domain processing was performed at the rate of $f_s = 36$ MHz.

We compare the performance of time domain processing to FDBF defined in (11) as well as to FDBF with different approximation levels in (14) according to the choice of N_q. The implementation of FDBF using (11) requires numerical computation of an integral and is not computationally practical. It is provided to verify the similarity between time and frequency domain processing when no approximations are applied. FDBF is performed at the effective bandpass bandwidth of the transmitted signal which is equal to 9 MHz.

To evaluate spatial resolution a tissue mimicking CIRS 040 GSE phantom with wire targets is used. The resulting images are shown in Fig. 3(a). The experimental axial and lateral point spread functions (PSF) are computed based on the response to a single point target at a depth of 21 mm and are presented in Fig. 4. As can be seen, axial resolution is not affected by frequency-domain implementation of beamforming for all approximation levels. The lateral resolution is also unchanged, however the lateral side-lobes are slightly higher for a coarse approximation, e.g. with $N_q = 5$. As expected, increased lateral side-lobes degrade the anechoic contrast computed based on the cyst scans, shown in Fig 3(b). The anechoic contrast is defined as

$$CR = \frac{\mu_{cyst} - \mu_b}{\sqrt{\sigma_{cyst}^2 + \sigma_b^2}}, \tag{17}$$

where $\mu_{cyst}, \sigma_{cyst}$ and μ_b, σ_b stand for the mean and standard deviation of log-compressed values of the cyst and the background, respectively. The computed values are presented in Table I. The contrast obtained by FDBF is 0.6 dB lower compared to time domain processing. One would expect similar performance for both methods since mathematically they are completely equivalent. This result can be explained by the fact that the implementation of FDBF according to (11) requires computation of an integral. When performed numerically such a computation introduces errors that affect the resulting performance. For FDBF with higher values of N_q, the contrast is still in good agreement with the one obtained by time domain processing.

In addition, the proposed method is validated with respect to a single beam corresponding to an image line and to the entire image after compounding. To compare the one-dimensional signals, we calculated the normalized root-mean-square error (NRMSE) between the signals obtained by FDBF and those obtained by standard beamforming in time. Both classes of signals were compared after envelope detection, performed by a Hilbert transform in order to remove the carrier. Denote by $\Phi[n;x_f]$ the signal obtained by standard beamforming and let $\hat{\Phi}[n;x_f]$ denote the signal obtained by beamforming in frequency. The Hilbert transform is denoted by $\mathcal{H}(\cdot)$. For the set of J image lines, we define NRMSE as:

$$NRMSE = \frac{1}{J}\frac{|\mathcal{H}(\Phi[n;x_f]) - \mathcal{H}(\hat{\Phi}[n;x_f])|_2}{\mathcal{H}(\Phi[n;x_f])_{\max} - \mathcal{H}(\Phi[n;x_f])_{\min}}, \tag{18}$$

where $\mathcal{H}(\Phi[n;x_f])_{\max}$ and $\mathcal{H}(\Phi[n;x_f])_{\min}$ denote the maximal and minimal values of the envelope of the beamformed signal in time.

Comparison of the resulting images in Fig. 3 was performed by calculating the structural similarity (SSIM) index [34], commonly used for measuring similarity between two images. Table II summarizes the resulting values. These values verify that both one-dimensional signals and the resulting images are extremely similar, even with a very coarse approximation with only five coefficients.

This article has been accepted for publication in a future issue of this journal, but has not been fully edited. Content may change prior to final publication. Citation information: DOI 10.1109/TUFFC.2018.2856301, IEEE Transactions on Ultrasonics, Ferroelectrics, and Frequency Control

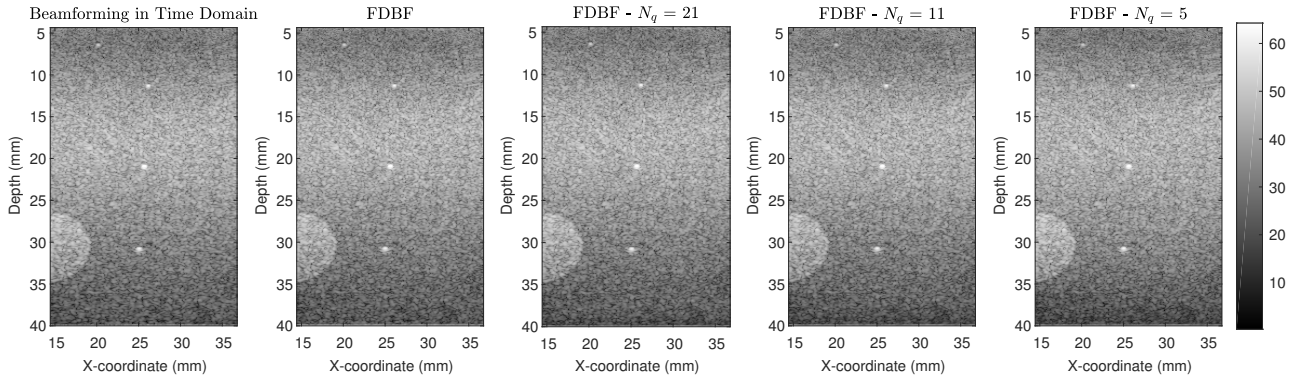

(a)

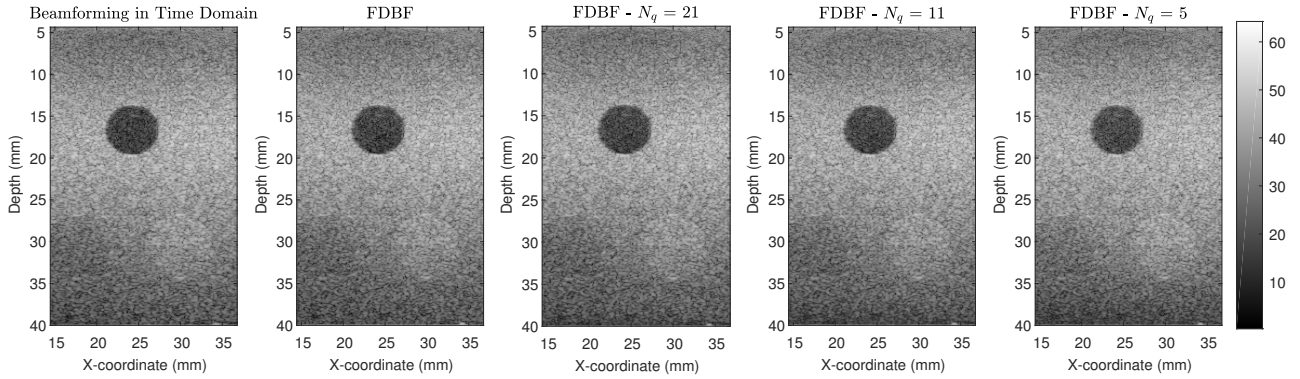

(b)

Fig. 3: Comparison of standard time domain processing and FDBF with different approximation levels. The first column from the left presents time domain processing while the second one corresponds to FDBF. The last three columns present FDBF with approximation using $N_q = 21, 11$ and 5 respectively. (a) Scan of wire targets for resolution evaluation. (b) Scan of anechoic cyst for contrast evaluation.

Table I: Anechoic Contrast

Method	Contrast, [dB]
Time Domain Beamforming	25.2
FDBF	24.6
FDBF, $N_q = 21$	24.2
FDBF, $N_q = 11$	23.7
FDBF, $N_q = 5$	22.5

Table II: NRMSE and SSIM

Medium	Method	SSIM	NRMSE
Wire targets	FDBF	0.920	0.057
	FDBF, $N_q = 21$	0.918	0.058
	FDBF, $N_q = 11$	0.913	0.060
	FDBF, $N_q = 5$	0.890	0.068
Cyst	FDBF	0.909	0.061
	FDBF, $N_q = 21$	0.900	0.062
	FDBF, $N_q = 11$	0.890	0.065
	FDBF, $N_q = 5$	0.880	0.070

IV. Low-Rate Acquisition and Sub-Nyquist Processing

We next address low-rate acquisition of Fourier coefficients of the detected signals required for frequency domain processing and show that the beamformed signal can be recovered from its partial frequency data while exploiting its structure.

A. Low-Rate Data Acquisition

The low-rate data acquisition step is based on the ideas of Xampling [12], [24], [25], which obtains the Fourier coefficients of individual detected signals from their low-rate samples. More specifically, using Xampling we can obtain an arbitrary set κ, comprised of K frequency components, from K point-wise samples of the signal filtered with an analog kernel $s(t)$, designed according to κ. In ultrasound imaging with modulated Gaussian pulses the transmitted signal has one main band of energy. As a result the analog filter takes on the form of a bandpass filter, leading to a simple low-rate sampling scheme [22]. The choice of κ dictates the bandwidth of the filter and the resulting sampling rate.

In plane-wave mode the same low-rate sampling scheme can be applied to the individual signals detected by the transducer elements yielding their Fourier coefficients. When all the beam's Fourier coefficients within its bandwidth are computed, the sampling and processing rates are equal to the effective

This article has been accepted for publication in a future issue of this journal, but has not been fully edited. Content may change prior to final publication. Citation information: DOI 10.1109/TUFFC.2018.2856301, IEEE Transactions on Ultrasonics, Ferroelectrics, and Frequency Control

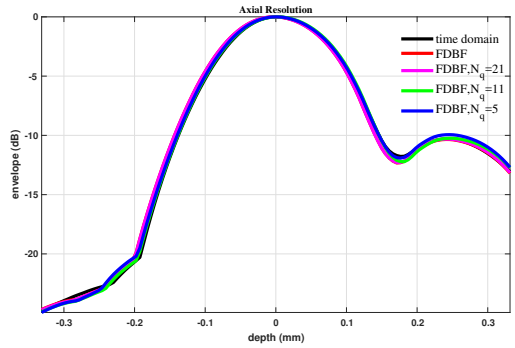

(a)

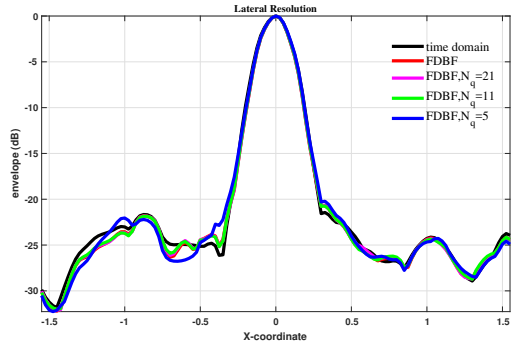

(b)

Fig. 4: Spatial resolution comparison for different processing methods. (a) Axial PSF. (b) Lateral PSF. The PSFs are computed empirically based on the response to a single point target with lateral and axial coordinates [25mm, 21 mm]. The legend is the same for both (a) and (b).

Nyquist rate. The beam in time is then obtained simply by an inverse Fourier transform. When further rate reduction is required, only a subset of Fourier coefficients is computed and the beam's structure is exploited to recover it from its partial frequency data.

B. Sparsity-Based Recovery from Partial Frequency Data

When FDBF is performed at a sub-Nyquist rate, the beamformed signal in time cannot be recovered by an inverse Fourier transform, since only partial frequency information is available. The ideas of sparsity of the beamformed signal combined with ℓ_1-regularized optimization were exploited in [20], [22]. There, clinical images were recovered from partial frequency data for a focused acquisition mode. In this work we follow these ideas and compensate for the apparent loss of information of sub-Nyquist processing by relying on sparsity of the beamformed data.

According to [20], the beamformed signal satisfies the finite rate of innovation (FRI) model [11], [35]. That is, we assume that it can be regarded as a sum of pulses, all replicas of a known transmitted pulse shape:

$$\Phi(t;x_f)=\sum_{l=1}^{L}\tilde{b}_l h(t-t_l). \tag{19}$$

Here $h(t)$ is the transmitted pulse, L is the number of scattering elements in the direction x_f, $\{\tilde{b}_l\}_{l=1}^{L}$ are the unknown amplitudes of the reflections and $\{t_l\}_{l=1}^{L}$ are the times at which the reflection from the l-th scatterer arrives at the reference element.

Having acquired the Fourier coefficients $c[k]$ as described in the previous section, we now wish to reconstruct the beamformed signal. Since the beam satisfies the FRI model our task is to extract the unknown parameters, $\{\tilde{b}_l\}_{l=1}^{L}$ and $\{t_l\}_{l=1}^{L}$, that describe it.

Denote $T_s=\frac{1}{f_s}$ and $N=T/T_s$. As shown in [22], when the delays $\{t_l\}_{l=1}^{L}$ are quantized with a step size T_s, such that $t_l=q_lT_s$ for some integer $0\le q_l\le N-1$, the Fourier coefficients of $\Phi(t;x_f)$ are given by

$$\begin{aligned}c[k]&=\frac{1}{T}\int_0^T\Phi(t;x_f)e^{-i\frac{2\pi}{T}kt}dt\\&=h[k]\sum_{j=0}^{N-1}b_je^{-i\frac{2\pi}{N}kj}.\end{aligned} \tag{20}$$

Here $h[k]$ is the k-th Fourier coefficient of $h(t)$ and $b_j=\tilde{b}_l\delta_{j,q_l}$ where $\delta_{a,b}$ is the Kronecker delta.

We conclude that recovering the beamformed signal in time is equivalent to determining b_l in (20) for $0\le l\le N-1$. In vector-matrix notation, (20) can be rewritten as

$$\mathbf{c}=\mathbf{HDb}=\mathbf{Ab}, \tag{21}$$

where $\mathbf{c}$ is a vector of length K with k-th entry $c[k]$, $\mathbf{H}$ is a $K\times K$ diagonal matrix with k-th entry $h[k]$, $\mathbf{D}$ is a $K\times N$ matrix whose rows are taken from the $N\times N$ DFT matrix corresponding to the relevant Fourier indices of $\Phi(t;x_f)$, and $\mathbf{b}$ is a column vector of length N with l-th entry b_l.

To extract the values of $\mathbf{b}$, which fully describe the beamformed signal, we rely on the assumption that a typical ultrasound image is relatively sparse or compressible. Namely, it is comprised of a small number of strong reflectors and much weaker sub-wavelength scatterers in the scanned tissue. Using this sparsity assumption we then find $\mathbf{b}$ by solving an ℓ_1 optimization problem:

$$\min_{\mathbf{b}}\|\mathbf{b}\|_1 \text{ s.t. } \|\mathbf{Ab}-\mathbf{c}\|_2\le\varepsilon. \tag{22}$$

In practice, we solve (22) using the NESTA algorithm [36] which works well when the signal of interest has high dynamic range. NESTA uses a single smoothing parameter, μ, selected based on a trade-off between accuracy and speed of convergence. We choose this parameter empirically to achieve good performance with respect to image quality.

C. Results

1) In vitro: To verify the performance of our sub-Nyquist technique we processed the data at the rate of 3.6 MHz which corresponds to 0.4 of the effective Nyquist rate and is 10 times lower than the minimal rate required for time domain beamforming. The processing rate is chosen empirically to be as low as possible while allowing to recover meaningful images. In the context of Xampling, defined in Section IV-A, the chosen processing rate corresponds to an analog preprocessing

This article has been accepted for publication in a future issue of this journal, but has not been fully edited. Content may change prior to final publication. Citation information: DOI 10.1109/TUFFC.2018.2856301, IEEE Transactions on Ultrasonics, Ferroelectrics, and Frequency Control

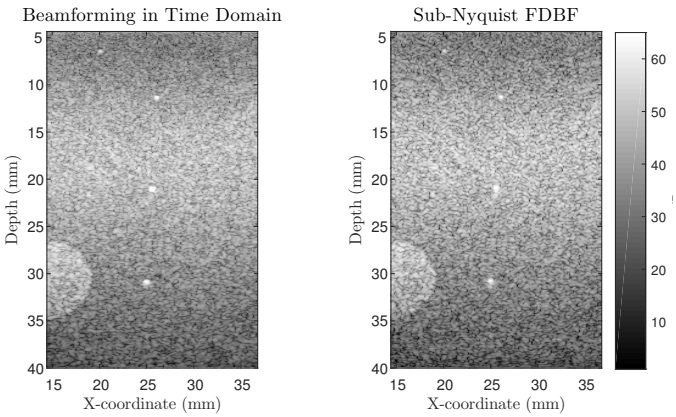

(a) (b)

Fig. 5: Scan of wire targets for resolution evaluation. (a) Time domain beamforming, processed at 36 MHz. (b) Sub-Nyquist FDBF, processed at 3.6 MHz.

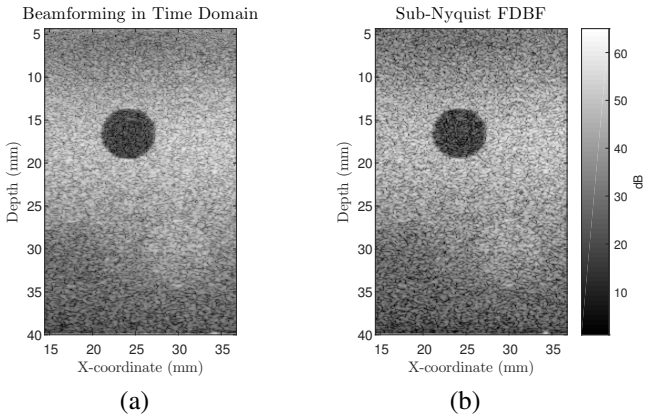

(a) (b)

Fig. 7: Scan of an anechoic cyst for contrast evaluation. (a) Time domain beamforming, processed at 36 MHz, anechoic contrast: 25.2 dB (b) Sub-Nyquist FDBF, processed at 3.6 MHz, anechoic contrast: 24.8 dB.

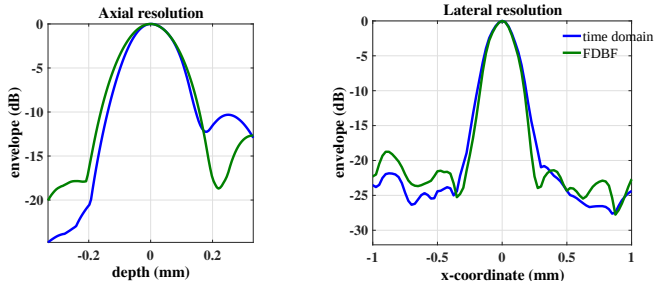

(a) (b)

Fig. 6: Spatial resolution comparison for time domain processing and sub-Nyquist FDBF. (a) Axial PSF. (b) Lateral PSF. The PSFs are computed empirically based on the response to a single point target with lateral and axial coordinates [25mm, 21 mm]. The legend is the same for both (a) and (b).

filter with bandwidth of 3.6 MHz centered around the central frequency of the transducer, $f_c = 9$ MHz. All the images are obtained with 41 transmitted plane-waves, as described in Section III-B. Spatial resolution is evaluated based on the wire targets scan presented in Fig. 5. The axial and lateral PSF, computed based on a point target 21 mm, are presented in Fig. 6. Contrast, evaluated based on the cyst scans shown if Fig. 7, is in good agreement for both methods. Corresponding values of NRMSE and SSIM are reported in the first two lines of Table III. These values validate close similarity between FDBF and sub-Nyquist FDBF. However, in this case, NRMSE is slightly higher and SSIM is lower, compared with the values obtained in Section III.

Table III: Sub-Nyquist FDBF: NRMSE and SSIM

Medium	SSIM	NRMSE
Wire targets	0.844	0.06
Cyst	0.796	0.08
Carotid (*in vivo*)	0.764	0.07
Thyroid (*in vivo*)	0.803	0.07

2) in vivo: We next applied sub-Nyquist FDBF to *in vivo* carotid artery data, obtained by scanning a healthy volunteer. The examination of the carotid wall is a powerful tool for atherosclerosis diagnosis and ultrasound imaging is one of the best methods for evaluation of the wall structure [37]. Intima-media (IM), defined as a double line pattern on both walls of the carotid artery, is a structure of interest for diagnosis. It can be seen from comparison of the highlighted boxes in Fig. 8 (a) and (b), that IM is preserved by FDBF and can be used for further diagnosis. Moreover, we note that despite a slight degradation of axial resolution, that can be noticed in Fig. 6 (a), the *in vivo* image retains all the fine details. This can be explained by the fact that the underlying clinical image contains fewer strong reflectors and thus, better fits the sparsity model.

We verify the ability of (22) to capture speckle by applying sub-Nyquist FDBF to *in vivo* data, obtained by scanning a healthy volunteer at the thyroid region. The scanned area includes soft tissue with almost no strong reflectors and, thus, is expected to provide an image comprised of fully developed speckle. The resulting images, shown in Fig. 9(a) and (b), demonstrate high similarity of the pattern resulting from time and frequency domain processing. An example of a RF image line obtained by both methods is presented in Fig. 10. It can be seen that the RF lines are very close even in the regions with weak echoes, that are expected to be speckle.

To provide statistical evidence that the resulting pattern is indeed speckle we check whether it obeys a Rayleigh probability density function (pdf) [38], [39] by performing a Kolmogorov-Smirnov (K-S) test. This is a common statistical hypothesis test that verifies whether there is enough evidence in the data to deduce that the hypothesis under consideration is correct. To this end, the envelope data of each image is divided to overlapping patches of 20×15 pixels and the K-S test is applied to each patch. The patches that pass the K-S test with significance level $\alpha = 0.05$ are included into the speckle region of each image. Figures 9(c) and (d) present the speckle regions obtained by time domain beamforming

This article has been accepted for publication in a future issue of this journal, but has not been fully edited. Content may change prior to final publication. Citation information: DOI 10.1109/TUFFC.2018.2856301, IEEE Transactions on Ultrasonics, Ferroelectrics, and Frequency Control

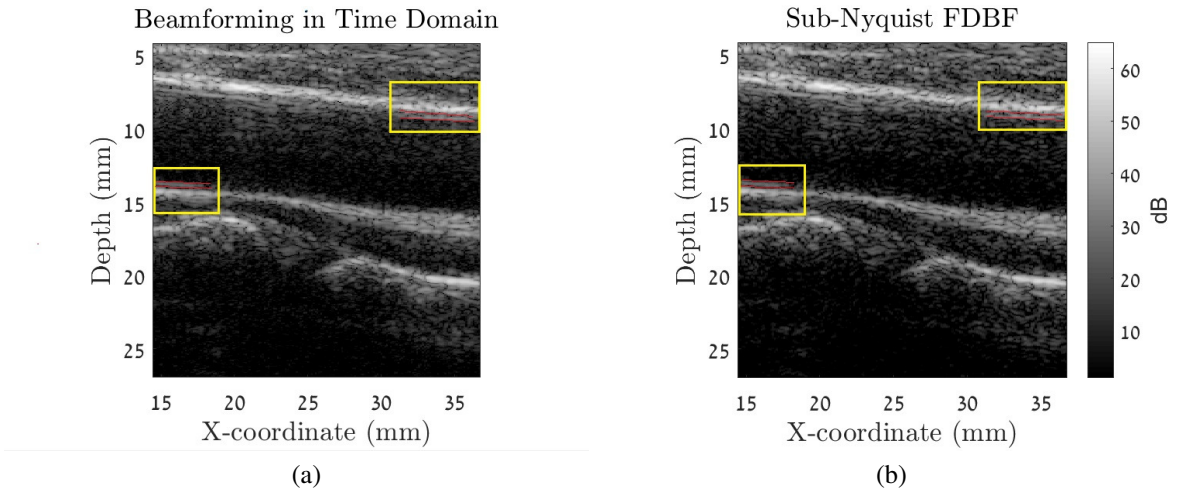

Fig. 8: *In vivo* carotid scan. The highlighted boxes contain the IM regions. (a) Time domain beamforming, processed at 36 MHz. (b) Sub-Nyquist FDBF, processed at 3.6 MHz.

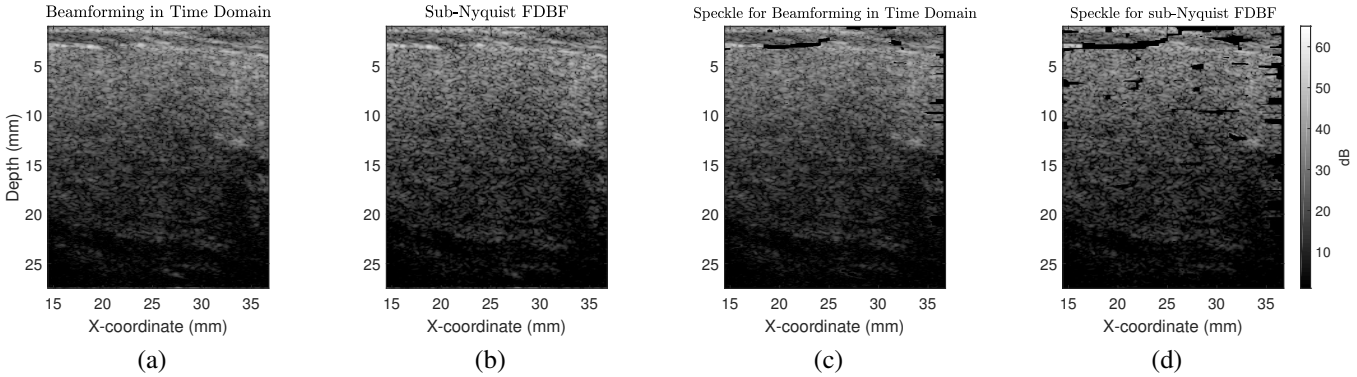

Fig. 9: *In vivo* thyroid scan. (a) Time domain beamforming, processed at 36 MHz, (b) sub-Nyquist FDBF, processed at 3.6 MHz, (c) speckle regions according to K-S test for time domain processing at 36 MHz, (d) speckle regions according to K-S test for time domain processing at 3.6 MHz.

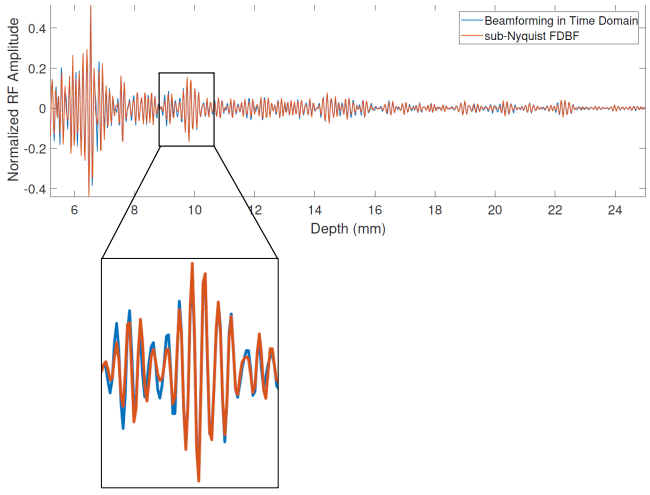

Fig. 10: Comparison of RF lines located at $x = 27$ mm from the thyroid scan presented in Fig. 9 obtained by time domain processing and sub-Nyquist FDBF.

and sub-Nyquist FDBF, respectively. The patches that did not pass the test are zeroed out. As expected, most of the image in Fig. 9(a) is indeed speckle. Speckle region in the image obtained by sub-Nyquist FDBF is in a good agreement with that of time domain processing. To quantify this similarity, we define the speckle region of time domain processing as a reference and compute which percentage of it is defined as speckle in an image obtained by the proposed method. The correspondence between the speckle regions in Figs. 9(c) and (d) is 95.7%, which clearly shows the ability of sub-Nyquist FDBF combined with an ℓ_1-based prior to recover speckle patterns.

The last two lines of Table III report the values of NRMSE and SSIM which correspond to applying sub-Nyquist FBDF on *in-vivo* carotid and thyroid data, showing similar results to those obtained using the phantom scans. We emphasize that the values of NRMSE and SSIM are provided to give a sense of performance of the proposed method compared with the established technique of time domain beamforming. In practice, validation is typically performed visually by sonographers, radiologists, and physicians. Furthermore, since

This article has been accepted for publication in a future issue of this journal, but has not been fully edited. Content may change prior to final publication. Citation information: DOI 10.1109/TUFFC.2018.2856301, IEEE Transactions on Ultrasonics, Ferroelectrics, and Frequency Control

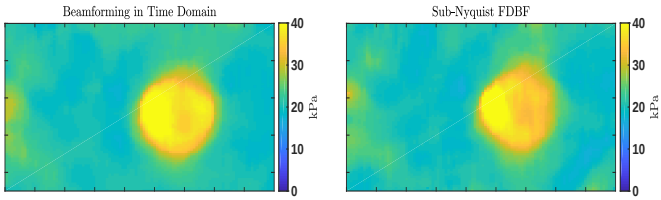

(a) (b)

Fig. 11: Elasticity maps of a phantom containing a 6 mm hard inclusion. (a) Time domain beamforming, processed at 30 MHz. (b) Sub-Nyquist FDBF, processed at 5 MHz.

our approach uses only a small portion of the spectrum, it inherently filters out noise, spread over the entire spectrum. Thus, high similarity with beamforming in time may not necessarily be advantageous.

3) Elastography: We next demonstrate the applicability of sub-Nyquist FDBF in velocity estimation. In particular, we consider supersonic shear imaging [2] where an Aixplorer system was used to scan a CIRS 040GSE phantom with an elasticity target of 40 kPa and 0 dB grayscale compared to the background. Three steered plane-waves were used for imaging and sub-Nyquist FDBF was applied on the data acquired for each of them. Inclusion detection was performed using shear compound as described in [2] and the resulting elasticity maps are presented in Fig. 11. As can be seen, the elasticity maps generated using time domain beamforming and sub-Nyquist FDBF are similar and allow distinguishing the elasticity target. Using sub-Nyquist FDBF the data is processed at the rate of 5 MHz which is 6 times lower than the rate of 30 MHz, required by time domain beamforming. This shows the potential use of sub-Nyquist FDBF for velocity estimation.

V. Discussion and Conclusions

In this work we extended the FDBF framework developed recently for focused imaging to plane-wave imaging and showed that the core of FDBF, the relationship between the beam and the detected signals in the frequency domain, holds. By appropriate modification of the distortion function that was originally derived for a focused mode to translate the beamforming delays to frequency, we extended FDBF to include dynamic aperture and apodization, crucial for image quality improvement. The efficient implementation of FDBF is enabled by approximation based on the decay properties of the distortion function. Here we verify numerically that the decay property is preserved in the case of Hamming apodization and evaluate the performance of FDBF for different approximation levels. Such a numerical study can be performed for any choice of the apodization function.

The effect of approximation on image quality is studied by measuring spatial resolution and contrast as well as SSIM and NRMSE values using real data acquired by a commercial scanner. The results verify the equivalence of time and frequency domain processing. We show that FDBF provides 4 times rate reduction by avoiding oversampling required by digital implementation of beamforming in time.

When the signal's structure is exploited further rate reduction is obtained. In this case we compute only a portion of the beam's bandwidth, which implies sampling and processing the detected signals at a sub-Nyquist rate. The recovery of the beam from its partial frequency data is then performed by solving an optimization problem under the assumption that the signal is compressible. The performance of sub-Nyquist processing is verified in terms of spatial resolution and contrast. Despite the slight degradation in axial resolution observed in measuring the PSF based on a tissue mimicking phantom, the comparison of *in vivo* carotid scans shows high similarity and the ability of the proposed method to recover the speckle pattern is verified using an *in vivo* thyroid scan. In addition, we demonstrate the use of sub-Nyquist FDBF to SWE. The ability to achieve significant rate reduction using sub-Nyquist FDBF while obtaining meaningful elasticity maps is of great importance since SWE is one of the main applications of ultrafast imaging.

Besides the immediate advantage of sampling and processing rate reduction, the proposed method offers two additional benefits. First, the reduction in the number of samples taken at each transducer element is a potential enabler for the concept of a wireless probe and remote processing [9]. Second, FDBF can efficiently incorporate pulse compression required for coded excitation imaging [40], [41]. Transmission of coded signals such as linear frequency modulated chirps yields increased SNR and penetration depth and was shown to improve the performance of shear-wave detection with plane wave imaging [42].

Appendix - Distortion Function

To derive an expression of the distortion function we consider two cases.

1) $\alpha = 0$: In this case we have

$$\tau_m(t; x_f, 0) = \frac{1}{2}\left(t + \sqrt{t^2 + 4\delta_{fm}^2}\right). \tag{23}$$

Defining $t' = \tau_m(t; x_f, 0)$, we obtain

$$\begin{aligned} t &= t' - \frac{\delta_{fm}^2}{t'}, \\ dt &= \left(1 + \frac{\delta_{fm}^2}{t'^2}\right) dt'. \end{aligned} \tag{24}$$

Using (24) we can write

$$\begin{aligned} &\varphi_m^0(\tau_m(t; x_f, 0)) = \varphi_m^0(t'), \\ &w_m(t; x_f) = w_m(t' - \frac{\delta_{fm}^2}{t'}; x_f), \\ &e^{-i\frac{2\pi}{T}kt} = e^{i\frac{2\pi}{T}k\frac{\delta_{fm}^2}{t'}} e^{-i\frac{2\pi}{T}kt'}, \\ &I_{[0, T_B(x_f))}(t) = I_{[\delta_{fm}, T_B'(x_f;0))}(t'), \end{aligned} \tag{25}$$

where $T_B^{'}(x_f; 0) \triangleq \tau_m(T_B(x_f); x_f, 0)$. Substituting $t' = \tau_m(t; x_f, 0)$ into (10) yields

This article has been accepted for publication in a future issue of this journal, but has not been fully edited. Content may change prior to final publication. Citation information: DOI 10.1109/TUFFC.2018.2856301, IEEE Transactions on Ultrasonics, Ferroelectrics, and Frequency Control

$$\hat{c}_m^0[k] = \frac{1}{T} \int_{\delta_{fm}}^{\tau_m(T;x_f,0)} \varphi_m^0(t') q_{k,m}(t';x_f,0) e^{-i\frac{2\pi}{T}kt'} dt', \quad (26)$$

where $q_{k,m}(t';x_f,0)$ is defined in (27). By construction, $T_B^{'}(x_f;0) \leq T$. Hence, considering the contribution of $I_{[\delta_{fm},T_B'(x_f;0))}(t')$, we can change the bounds of integration in (26) to get

$$\hat{c}_m^0[k] = \frac{1}{T} \int_0^T \varphi_m^0(t') q_{k,m}(t';x_f,0) e^{-i\frac{2\pi}{T}kt'} dt'. \quad (28)$$

Omitting the tag superscript in t', for clarity, results in equation (11) where $\alpha = 0$.

2) $\alpha \neq 0$: Define $t' = \tau_m(t;x_f,\alpha)$ and let $y = 2\left(t' - \frac{x_f \sin\alpha}{c}\right)$. We then obtain

$$\begin{aligned} t &= \frac{-y\cos\alpha + \sqrt{y^2 - 4\delta_{fm}^2 \sin^2\alpha}}{\sin^2\alpha}, \\ dt &= \frac{2(y - t'\cos\alpha)}{\sqrt{y^2 - 4\delta_{fm}^2\sin^2\alpha}} dt'. \end{aligned} \quad (29)$$

Substituting the latter into (10) we have

$$\hat{c}_m^\alpha[k] = \frac{1}{T} \int_{\frac{x_f\sin\alpha}{c}+\delta_{fm}}^{\tau_m(T;x_f,\alpha)} \varphi_m^\alpha(t') q_{k,m}(t';x_f,\alpha) e^{-i\frac{2\pi}{T}kt'} dt', \quad (30)$$

where $q_{k,m}(t';x_f,\alpha)$ is given by (31) and we define $T_B^{'}(x_f;\alpha) \triangleq \tau_m(T_B(x_f);x_f,\alpha)$. An explicit expression of the distortion function for Hamming window apodization, defined in (13), is presented in (32). As in the previous case, it holds that $T_B^{'}(x_f;\alpha) \leq T$. Taking into account the indicator function $I_{[\frac{x_f\sin\alpha}{c}+\delta_{fm},T_B'(x_f;\alpha))}(t')$, we can modify (30) to get equation (11).

ACKNOWLEDGMENT

The authors thank Prof. Mathias Fink for many insightful discussions.

REFERENCES

[1] L. Sandrin, S. Catheline, M. Tanter, X. Hennequin, and M. Fink, "Time-resolved pulsed elastography with ultrafast ultrasonic imaging," *Ultrasonic Imaging*, vol. 21, no. 4, pp. 259–272, 1999.

[2] J. Bercoff, M. Tanter, and M. Fink, "Supersonic shear imaging: a new technique for soft tissue elasticity mapping," *IEEE Transactions on Ultrasonics, Ferroelectrics and Frequency Control*, vol. 51, no. 4, pp. 396–409, 2004.

[3] G. Montaldo, M. Tanter, J. Bercoff, N. Benech, and M. Fink, "Coherent plane-wave compounding for very high frame rate ultrasonography and transient elastography," *IEEE Transactions on Ultrasonics, Ferroelectrics and Frequency Control*, vol. 56, no. 3, pp. 489–506, 2009.

[4] B. D. Steinberg, "Digital beamforming in ultrasound," *IEEE Transactions on Ultrasonics, Ferroelectrics and Frequency Control*, vol. 39, no. 6, pp. 716–721, 1992.

[5] O. D. Grace and S. P. Pitt, "Sampling and interpolation of bandlimited signals by quadrature methods," *The Journal of the Acoustical Society of America*, vol. 48, no. 6A, pp. 1311–1318, 1970.

[6] J. Ophir, S. K. Alam, B. Garra, F. Kallel, E. Konofagou, T. Krouskop, and T. Varghese, "Elastography: ultrasonic estimation and imaging of the elastic properties of tissues," *Proceedings of the Institution of Mechanical Engineers, Part H: Journal of Engineering in Medicine*, vol. 213, no. 3, pp. 203–233, 1999.

[7] M. Tanter and M. Fink, "Ultrafast imaging in biomedical ultrasound," *IEEE Transactions on Ultrasonics, Ferroelectrics, and Frequency Control*, vol. 61, no. 1, pp. 102–119, 2014.

[8] M. Omidyeganeh, Y. Xiao, M. O. Ahmad, and H. Rivaz, "Estimation of strain elastography from ultrasound radio-frequency data by utilizing analytic gradient of the similarity metric," *IEEE Transactions on Medical Imaging*, vol. 36, no. 6, pp. 1347–1358, 2017.

[9] A. Eilam, T. Chernyakova, Y. C. Eldar, and A. Kempinski, "Sub-Nyquist medical ultrasound imaging: En route to cloud processing," in *Global Conference on Signal and Information Processing (GlobalSIP)*. IEEE, 2013, pp. 1017–1020.

[10] Y. C. Eldar, *Sampling Theory: Beyond Bandlimited Systems*. Cambridge University Press, 2015.

[11] Y. C. Eldar and G. Kutyniok, *Compressed sensing: theory and applications*. Cambridge University Press, 2012.

[12] R. Tur, Y. C. Eldar, and Z. Friedman, "Innovation rate sampling of pulse streams with application to ultrasound imaging," *IEEE Transactions on Signal Processing*, vol. 59, no. 4, pp. 1827–1842, 2011.

[13] X. Zhuang, Y. Zhao, Z. Dai, H. Wang, and L. Wang, "Ultrasonic signal compressive detection with sub-nyquist sampling rate," *Journal of Scientific and Industrial Research*, vol. 71, pp. 195–199, 2012.

[14] J. Zhou, S. Hoyos, and B. M. Sadler, "Asynchronous compressed beamformer for portable diagnostic ultrasound systems," *IEEE Transactions on Ultrasonics, Ferroelectrics and Frequency Control*, vol. 61, no. 11, pp. 1791–1801, 2014.

[15] H. Liebgott, R. Prost, and D. Friboulet, "Pre-beamformed rf signal reconstruction in medical ultrasound using compressive sensing," *Ultrasonics*, vol. 53, no. 2, pp. 525–533, 2013.

[16] A. Achim, A. Basarab, G. Tzagkarakis, P. Tsakalides, and D. Kouamé, "Reconstruction of ultrasound rf echoes modeled as stable random variables," *IEEE Transactions on Computational Imaging*, vol. 1, no. 2, pp. 86–95, 2015.

[17] G. Tzagkarakis, A. Achim, P. Tsakalides, and J.-L. Starck, "Joint reconstruction of compressively sensed ultrasound rf echoes by exploiting temporal correlations," in *International Symposium on Biomedical Imaging (ISBI)*. IEEE, 2013, pp. 632–635.

[18] C. Quinsac, A. Basarab, and D. Kouamé, "Frequency domain compressive sampling for ultrasound imaging," *Advances in Acoustics and Vibration*, vol. 12, pp. 1–16, 2012.

[19] O. Lorintiu, H. Liebgott, M. Alessandrini, O. Bernard, and D. Friboulet, "Compressed sensing reconstruction of 3D ultrasound data using dictionary learning and line-wise subsampling," *IEEE Transactions on Medical Imaging*, vol. 34, no. 12, pp. 2467–2477, 2015.

[20] N. Wagner, Y. C. Eldar, and Z. Friedman, "Compressed beamforming in ultrasound imaging," *IEEE Transactions on Signal Processing*, vol. 60, no. 9, pp. 4643–4657, 2012.

[21] M. F. Schiffner and G. Schmitz, "A low-rate parallel Fourier domain beamforming method for ultrafast pulse-echo imaging," in *International Ultrasonics Symposium (IUS)*. IEEE, 2016, pp. 1–4.

[22] T. Chernyakova and Y. C. Eldar, "Fourier domain beamforming: The path to compressed ultrasound imaging," *IEEE Transactions on Ultrasonics, Ferroelectrics, and Frequency Control*, vol. 61, no. 8, pp. 1252–1267, 2014.

[23] A. Burshtein, M. Birk, T. Chernyakova, A. Eilam, A. Kempinski, and Y. C. Eldar, "Sub-Nyquist sampling and Fourier domain beamforming in volumetric ultrasound imaging," *IEEE Transactions on Ultrasonics, Ferroelectrics, and Frequency Control*, vol. 63, no. 5, pp. 703–716, 2016.

[24] K. Gedalyahu, R. Tur, and Y. C. Eldar, "Multichannel sampling of pulse streams at the rate of innovation," *IEEE Transactions on Signal Processing*, vol. 59, no. 4, pp. 1491–1504, 2011.

[25] E. Baransky, G. Itzhak, I. Shmuel, N. Wagner, E. Shoshan, and Y. C. Eldar, "Sub-nyquist radar prototype: Hardware and algorithm," *IEEE Transactions on Aerospace and Electronic Systems*, vol. 50, no. 2, pp. 809–822, 2014.

[26] R. Cohen, Y. Sde Chen, T. Chernyakova, C. Fraschini, J. Bercoff, and Y. C. Eldar, "Fourier domain beamforming for coherent plane-wave compounding," in *International Ultrasonics Symposium (IUS)*. IEEE, 2015, pp. 1–4.

[27] C. E. Thomas, "Dynamic array aperture and focus control for ultrasonic imaging systems," Dec. 25 1979, uS Patent 4,180,790.

This article has been accepted for publication in a future issue of this journal, but has not been fully edited. Content may change prior to final publication. Citation information: DOI 10.1109/TUFFC.2018.2856301, IEEE Transactions on Ultrasonics, Ferroelectrics, and Frequency Control

$$q_{k,m}(t';x_f,0) \triangleq w_m\left(t'-\frac{\delta_{fm}^2}{t'};x_f\right)\cdot I_{[\delta_{fm},T_B'(x_f;0))}(t')\cdot\left(1+\frac{\delta_{fm}^2}{t'^2}\right)\cdot\exp\left\{i\frac{2\pi}{T}k\frac{\delta_{fm}^2}{t'}\right\}. \tag{27}$$

$$\begin{aligned} q_{k,m}(t';x_f,\alpha) \triangleq & w_m\left(\frac{-y\cos\alpha+\sqrt{y^2-4\delta_{fm}^2\sin^2\alpha}}{\sin^2\alpha};x_f\right)\cdot I_{[\frac{x_f\sin\alpha}{c}+\delta_{fm},T_B'(x_f;\alpha))}(t')\cdot \\ & \frac{2(y-t'\cos\alpha)}{\sqrt{y^2-4\delta_{fm}^2\sin^2\alpha}}\cdot\exp\left\{i\frac{2\pi}{T}k\left(\frac{-y\cos\alpha+\sqrt{y^2-4\delta_{fm}^2\sin^2\alpha}}{\sin^2\alpha}+t'\right)\right\}. \end{aligned} \tag{31}$$

$$\begin{aligned} q_{k,m}(t;x_f,\alpha) = & \frac{2f\#}{c(a^2+0.5b^2)}\cdot\frac{\sin^2\alpha}{-y\cos\alpha+\sqrt{y^2-4\delta_{fm}^2\sin(\alpha)^2}}\cdot\left[a+b\cos\left(\frac{4\pi f\#\delta_{fm}\sin^2\alpha}{-y\cos\alpha+\sqrt{y^2-4\delta_{fm}^2\sin^2\alpha}}\right)\right]\cdot \\ & \frac{2}{\sin^2\alpha}\left[\frac{y}{\sqrt{y^2-4\delta_{fm}^2\sin^2\alpha}}-\cos\alpha\right]\cdot\exp\left\{-i\frac{2\pi}{T}k\frac{-y\cos\alpha+\sqrt{y^2-4\delta_{fm}^2\sin^2\alpha}}{\sin^2\alpha}\right\}\cdot\exp\left\{-i\frac{2\pi}{T}kt\right\}\cdot \\ & \mathrm{H}\left(\frac{-y\cos\alpha+\sqrt{y^2-4\delta_{fm}^2\sin^2\alpha}}{\sin^2\alpha}-4f\#\delta_{fm}\right). \end{aligned} \tag{32}$$

[28] M. Schiffner, T. Jansen, and G. Schmitz, "Compressed sensing for fast image acquisition in pulse-echo ultrasound," *Biomedical Engineering*, vol. 57, no. SI-1 Track-B, pp. 192–195, 2012.

[29] G. David, J.-l. Robert, B. Zhang, and A. F. Laine, "Time domain compressive beam forming of ultrasound signals," *The Journal of the Acoustical Society of America*, vol. 137, no. 5, pp. 2773–2784, 2015.

[30] A. Besson, M. Zhang, F. Varray, H. Liebgott, D. Friboulet, Y. Wiaux, J.-P. Thiran, R. E. Carrillo, and O. Bernard, "A sparse reconstruction framework for Fourier-based plane-wave imaging," *IEEE Transactions on Ultrasonics, Ferroelectrics, and Frequency Control*, vol. 63, no. 12, pp. 2092–2106, 2016.

[31] J.-Y. Lu and J. F. Greenleaf, "Pulse-echo imaging using a nondiffracting beam transducer," *Ultrasound in Medicine & Biology*, vol. 17, no. 3, pp. 265–281, 1991.

[32] ——, "Ultrasonic nondiffracting transducer for medical imaging," *IEEE Transactions on Ultrasonics, Ferroelectrics, and Frequency Control*, vol. 37, no. 5, pp. 438–447, 1990.

[33] W. D. OBrien, "Ultrasound–biophysics mechanisms," *Progress in Biophysics and Molecular Biology*, vol. 93, no. 1, pp. 212–255, 2007.

[34] Z. Wang, A. C. Bovik, H. R. Sheikh, and E. P. Simoncelli, "Image quality assessment: From error visibility to structural similarity," *IEEE Transactions on Image Processing*, vol. 13, no. 4, pp. 600–612, 2004.

[35] M. Vetterli, P. Marziliano, and T. Blu, "Sampling signals with finite rate of innovation," *IEEE Transactions on Signal Processing*, vol. 50, no. 6, pp. 1417–1428, 2002.

[36] S. Becker, J. Bobin, and E. J. Candès, "NESTA: a fast and accurate first-order method for sparse recovery," *SIAM Journal on Imaging Sciences*, vol. 4, no. 1, pp. 1–39, 2011.

[37] I. Simova, "Intima-media thickness: Appropriate evaluation and proper measurement, described," *E-journal of the ESC Council for Cardiology Practice*, vol. 13, 2015.

[38] C. B. Burckhardt, "Speckle in ultrasound b-mode scans," *IEEE Transactions on Sonics and Ultrasonics*, vol. 25, no. 1, pp. 1–6, 1978.

[39] R. F. Wagner, S. W. Smith, J. M. Sandrik, and H. Lopez, "Statistics of speckle in ultrasound b-scans." *IEEE Transactions on Sonics and Ultrasonics*, vol. 30, no. 3, pp. 156–163, 1983.

[40] A. Lahav, Y. Ben-Shalom, T. Chernyakova, and Y. C. Eldar, "Coded excitation ultrasound: Efficient implementation via frequency domain processing," in *International Conference on Acoustics, Speech and Signal Processing (ICASSP)*. IEEE, 2016, pp. 674–678.

[41] A. Lahav, T. Chernyakova, and Y. C. Eldar, "Focus: Fourier-based coded ultrasound," *IEEE Transactions on Ultrasonics, Ferroelectrics, and Frequency Control*, vol. 64, no. 12, pp. 1828–1839, 2017.

[42] P. Song, M. W. Urban, A. Manduca, J. F. Greenleaf, and S. Chen, "Coded excitation plane wave imaging for shear wave motion detection," *IEEE Transactions on Ultrasonics, Ferroelectrics, and Frequency Control*, vol. 62, no. 7, pp. 1356–1372, 2015.